

## Giant laser-induced resistive switching effect in Ag/TiO<sub>x</sub>/p-Si structures

Kang'an Jiang,<sup>1,2</sup> Yuhong Cao,<sup>1,2</sup> Dehui Huang,<sup>1,2</sup> Zhiyan Zheng,<sup>3</sup> Feiyu Ren,<sup>4</sup> Zhuyikang Zhao,<sup>1,2</sup>  
Su Hu,<sup>1,2</sup> Ke Chang,<sup>1,2</sup> Xinhui Zhao,<sup>1,2</sup> and Hui Wang<sup>1,2,\*</sup>

<sup>1</sup>*State Key Laboratory of Advanced Optical Communication Systems and Networks, School of Physics and Astronomy, Shanghai Jiao Tong University, 800 Dongchuan Road, Shanghai 200240, China*

<sup>2</sup>*Key Laboratory for Thin Film and Microfabrication Technology of the Ministry of Education, Research Institute of Micro/Nano Science and Technology, Shanghai Jiao Tong University, 800 Dongchuan Road, Shanghai 200240, China*

<sup>3</sup>*School of Biomedical Engineering, Shanghai Jiao Tong University, 800 Dongchuan Road, Shanghai 200240, China*

<sup>4</sup>*School of Mechanical Engineering, University of Shanghai for Science and Technology, Shanghai 200093, China*

(Received 13 March 2023; revised 10 April 2024; accepted 25 June 2024; published 12 July 2024)

Compared with traditional electric-field-controlled resistive random-access memory, optoelectronic resistive random-access memory (ORRAM) can be modulated in more dimensions by applying a laser; this is identified as a potential device to meet the demands of neuromorphic vision sensors. As a device with a wide range of application prospects, ORRAM still faces many challenges, such as an unclear mechanism and poor performance. Using the photosensitive properties of TiO<sub>2</sub> and the effects of the oxygen vacancy in anatase TiO<sub>2</sub>, we successfully obtain the giant laser-induced resistance effect in the Ag/TiO<sub>x</sub>/p-Si structure, and its electrical conductivity is enhanced by about 4000 times with a response time of less than 24 μs (the response time of most TiO<sub>2</sub> thin-film devices is in the order of milliseconds to seconds), which greatly improves the performance of ORRAM. This work provides a scalable strategy for the development of ORRAM devices and brings ORRAM closer to practical applications.

DOI: 10.1103/PhysRevApplied.22.014031

### I. INTRODUCTION

How to control the resistance state of a given material or a given structure is one of the important problems in physics research. Since Chua proposed the concept of memristors in 1971 [1], they have been widely studied as next-generation nonvolatile memories. Magnetoresistive random-access memory based on the magnetoresistance effect [2,3] has been fully developed. Resistive random-access memory is also a typical memristor based on the resistive switching (RS) effect [4,5]. Most current research focuses on modulating the resistance characteristics with an electric field [6–8], but there are a few studies on the laser-induced RS effect. Compared to the electroresistive switching effect, an optoelectronic resistive random-access memory (ORRAM) device can be modulated in more dimensions by applying a laser, making it possible to integrate the resistive switching device into neuromorphic vision sensors [9,10]. However, achieving the laser-induced RS effect is still challenging. Most successful examples are multicomponent compounds based on the Mo element, in which processes comparable to phase transitions occur [9,10]. This phase-transition effect depends

on the humidity and temperature of the environment and is limited to a few specific materials [11]. Such effects are also different from conductive-filament- (CF) based RS devices widely studied previously [5,12–14], which makes it difficult to extend the direction of material selection for laser-induced RS devices. Therefore, a high-quality laser-induced RS effect based on alternative mechanisms has been a bottleneck problem in this field.

Some highly researched materials with strong photosensitive characteristics, such as TiO<sub>2</sub>, are very suitable for use as storage layer materials for laser-induced RS devices, to break through the previous limitations of the electroresistive switching effect and providing a different idea for the study of laser-induced RS devices. Based on these photosensitive materials, we hope to use the research results for the electroresistive switching effect based on the CF-like mechanism to obtain an alternative strategy, which is different from phase-transition effects, to achieve a simpler operation and stronger effect of the laser-induced RS effect. In this work, the feasibility of this idea is verified by the oxygen-vacancy migration mechanism based on anatase TiO<sub>2</sub>, which provides a meaningful reference for the conversion of the electroresistive switching effect into the laser-induced RS effect. In addition, our work also provides a useful supplement to research on the photosensitive

\*Contact author: huiwang@sjtu.edu.cn

characteristics of  $\text{TiO}_2$ . Thanks to the transformative application of the mechanism of the electroresistive switching effect, we greatly improve the response speed of  $\text{TiO}_2$ -based photosensitive devices while maintaining a high switching ratio.

Here, we observed 405-nm light sensing and conductivity enhancement of over  $10^3$  times in a simple two-terminal structure of  $\text{Ag}/\text{TiO}_x/p\text{-Si}$ . A resistive switching mechanism based on the action of oxygen vacancies is proposed to support our work. The device has a response time of 24  $\mu\text{s}$ , and we show the application prospect of this fast response speed in Morse code transmission. Besides, the response of the device at multiple laser wavelengths has been tested, and the cyclic characteristics of the device are tested to demonstrate its reliability; this shows the potential of the  $\text{TiO}_x$ -based ORRAM for application in visual neural sensors. According to the response characteristics of the device to different laser wavelengths, we use a  $5 \times 5$  array to demonstrate its possible application in image processing. Compared with previous studies on  $\text{TiO}_x$ -based electroresistive switching effects [15–17], this work realized programming the device by laser stimulation, thus providing an alternative modulation scheme for  $\text{TiO}_x$ -based resistive switching devices.

## II. METHODS

### A. Device fabrication

The  $\text{TiO}_x$  films are grown on *p*-type Si substrates by radio-frequency magnetron sputtering. The Ag films are deposited by direct-current magnetron sputtering. Figure 1(a) is a cross-section scanning electron microscopy (SEM) image of the sample, where the  $\text{TiO}_x$  film is deposited for 30 min and the Ag film is deposited for 60 s. It shows the thicknesses of the  $\text{TiO}_x$  film and Ag film are 16 and 45 nm, respectively. So, the deposition rate can be calculated:  $8.9 \times 10^{-2} \text{ \AA/s}$  for  $\text{TiO}_x$  and  $7.5 \text{ \AA/s}$  for Ag. See the Supplemental Material [18] for more details on device fabrication.

### B. Characterization and measurements

The samples morphologies and microstructures were studied by field-emission scanning electron microscopy (ZEISS GeminiSEM 300), dispersive Raman microscopy (Senterra R200-L), UV–Vis–near-IR spectrophotometry (Shimadzu UV-3600i Plus), and x-ray photoelectron spectroscopy (XPS, ThermoFisher ESCALAB 250Xi). Electrical measurements were carried out using a Keithley 4200-SCS parameter analyzer, TTPX probe station, and WaveRunner 606Zi oscilloscope. The lasers involved in this work all have a power density of  $2 \text{ mW/cm}^2$ .

## III. RESULTS AND DISCUSSION

### A. Structural analysis

Confirming the specific structures of  $\text{TiO}_x$  will help to understand the resistance switching mechanism. Raman spectra are obtained with a 785-nm laser at room temperature. The results are shown in Fig. 1(b). The red curve is the Raman spectrum of the  $\text{TiO}_x$  film, and it shows several peaks caused by two different  $\text{TiO}_2$  structures and some impurities or defects. The green curve is a sketch of the rutile  $\text{TiO}_2$  Raman spectrum obtained from the red curve, and three Raman-active modes of the multiproton process ( $244 \text{ cm}^{-1}$ ),  $E_g$  ( $418 \text{ cm}^{-1}$ ), and  $A_{1g}$  ( $607 \text{ cm}^{-1}$ ) are observed, while the published work shows that these values are 235, 445, and  $610 \text{ cm}^{-1}$ , respectively [21,22]. The blue curve is a sketch of the anatase  $\text{TiO}_2$  Raman spectrum obtained from the red curve. In theory, four Raman-active modes of  $E_g$  ( $144 \text{ cm}^{-1}$ ),  $B_{1g}$  ( $400 \text{ cm}^{-1}$ ),  $A_{1g}$  ( $507 \text{ cm}^{-1}$ ), and  $E_g$  ( $635 \text{ cm}^{-1}$ ) should be observed for anatase  $\text{TiO}_2$ ; the peak at  $E_g$  ( $144 \text{ cm}^{-1}$ ) is stronger than the other three [21,22]. In this work, the spectrum of rutile  $\text{TiO}_2$  covers up the peaks of  $B_{1g}$  ( $400 \text{ cm}^{-1}$ ) and  $E_g$  ( $635 \text{ cm}^{-1}$ ) of anatase  $\text{TiO}_2$ , and only two peaks are left,  $E_g$  ( $145 \text{ cm}^{-1}$ ) and  $A_{1g}$  ( $503 \text{ cm}^{-1}$ ). Additionally, the Raman spectrum of rutile  $\text{TiO}_2$  may also mask the Raman spectrum of brookite  $\text{TiO}_2$  [23], which makes it impossible to infer whether there is brookite  $\text{TiO}_2$  structure in the  $\text{TiO}_x$  film. However, the existence of the brookite structure makes no contribution to the resistance switching effect mentioned later. In addition, it is noted that the presence of impurities and defects results in an offset of the actual Raman spectrum [24]. Therefore, there are some differences between the experimental data and the theoretical values, but the results show that the  $\text{TiO}_x$  film is composed of at least two kinds of structures, anatase and rutile.

### B. Laser-induced resistive switching effect

Optoelectronic memories can be programmed by laser stimulations and read out by electrical operations. Figure 1(c) shows a schematic illustration of the measurement circuit. For testing, the lateral two neighboring Ag electrodes are connected to the circuit. All electrical responses are measured using a Keithley 4200-scs parameter analyzer. The step of the sweeping voltage is 0.1 V and the sweeping process is 0 V–8 V–0 V. The positive electrode is stimulated by the laser to complete the light-response test. The transmittance of the Ag electrode is tested, as shown in Fig. S1 within the Supplemental Material [18]. It can be seen that the transmittance of the Ag electrode to the 405-nm laser is 19%. Therefore, the laser power density we use, which is  $2 \text{ mW/cm}^2$ , actually penetrates into the  $\text{TiO}_x$  film with a power density of about  $0.38 \text{ mW/cm}^2$ .

Figure 1(d) shows the results for one cycle in the test. The black curve is the initial state of the sample, which is

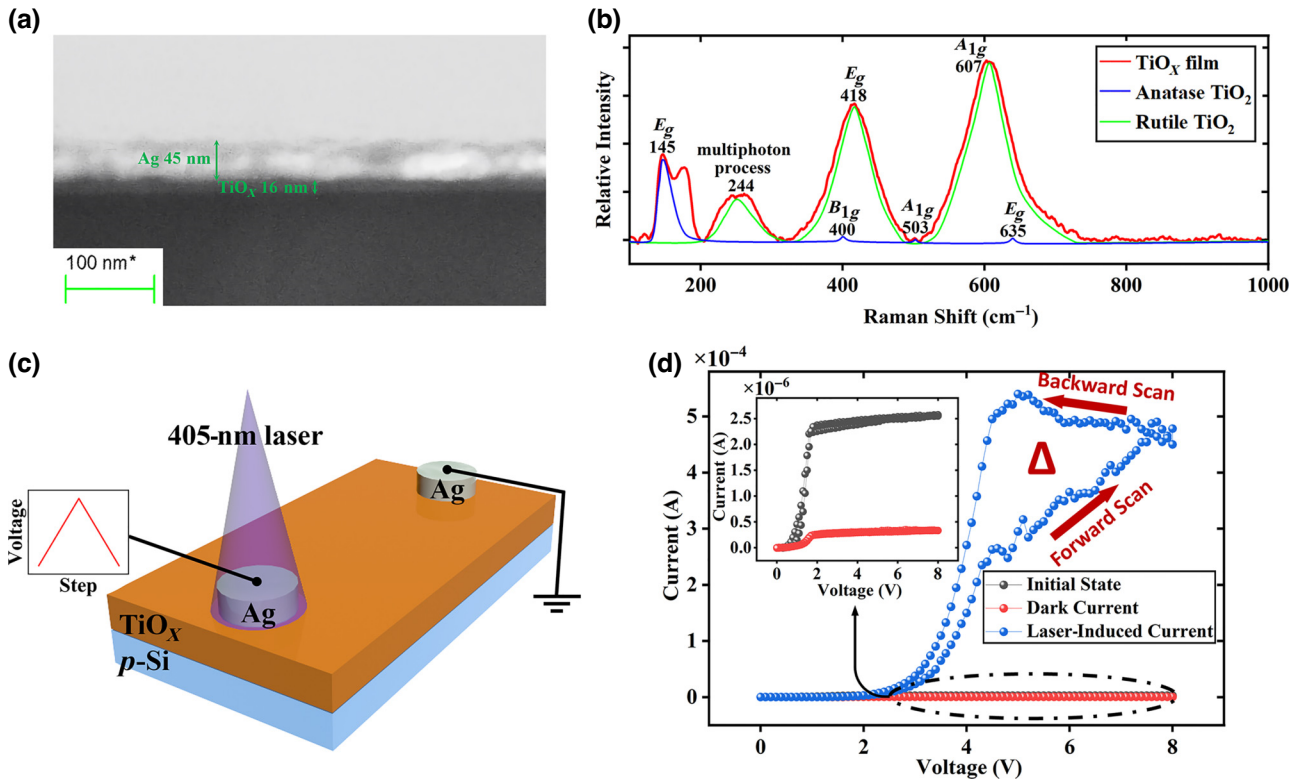


FIG. 1. (a) Cross-section SEM image of the Ag/TiO<sub>x</sub>/p-Si structure. (b) Red curve is the Raman spectrum of the TiO<sub>x</sub> film; blue and green curves are sketches of the anatase and rutile TiO<sub>2</sub> spectra obtained from the peaks of the red curve. (c) Schematic illustration of the measurement circuit. (d)  $I$ - $V$  curves of one cycle under a voltage-sweeping test. Inset shows a more detailed variation of the dark current and initial state under the voltage-sweeping test.

the  $I$ - $V$  curve of the freshly prepared sample without any laser modulation. In sharp contrast, the device is switched to a low-resistance state (LRS) under light illumination. The blue curve in Fig. 1(d) shows the result. Intriguingly, at positive voltage, there is a significant distinction between currents in forward and backward scans, showing a hysteresis property. It shows a higher resistance in the forward scan and a lower resistance in the backward scan. This hysteresis loop has a memory effect, which is consistent with the characteristics of a memristor [1,25,26]. This resistive switching effect is caused by the migration of oxygen vacancies in the TiO<sub>x</sub> film [15,16], which is discussed in detail later. After removing laser illumination, the device is switched to a high-resistance state (HRS), and the value of the resistance is even higher than the initial state, which is shown as the red curve in Fig. 1(d). The current obtained after removing illumination is defined as the dark current. It should be noted that the saturation current exists in the  $I$ - $V$  curves of all three cases because the carrier concentration transported between the two electrodes in the transverse direction reaches the upper limit. The saturation current of the laser-induced current and of the dark current are defined as  $I_{SL}$  and  $I_{SD}$ , respectively. It is found that the laser-to-dark ratio,  $I_{SL}/I_{SD}$ , is over  $10^3$ , which shows that the conductivity of the device will

be enhanced by more than  $10^3$  times under laser stimulation. This is a higher enhancement ratio than the previous work ( $10^0$ – $10^2$ ) [9,27,28]. To better describe the resistive switching characteristics, the parameter describing the level of the switching characteristic in a single  $I$ - $V$  test is set as the switching ratio,  $\Delta = \Sigma I_{back}/\Sigma I_{forward}$ ; here,  $\Sigma I$  is defined within the range of sweep voltage where the RS effect occurs, i.e.,  $\Sigma I_{forward}$  is the sum of the current under 0–8 V and  $\Sigma I_{back}$  is the sum of the current under 8–0 V.

### C. Mechanistic analysis

There are three questions that need to be clarified: (1) Why is the electrical conductivity of the device enhanced by more than  $10^3$  times under laser stimulation? (2) Why do new hysteretic characteristics appear under laser stimulation? (3) Why is the resistance value of the dark current higher than the initial state?

First, we try to understand how the laser-induced current is enhanced. We rule out the possibility of a photoresponse in the p-Si substrate. Figure S2 within the Supplemental Material [18] shows that the resistance state of the p-Si substrate does not change significantly under the action of a laser. Therefore, the effects of TiO<sub>x</sub> films need to be

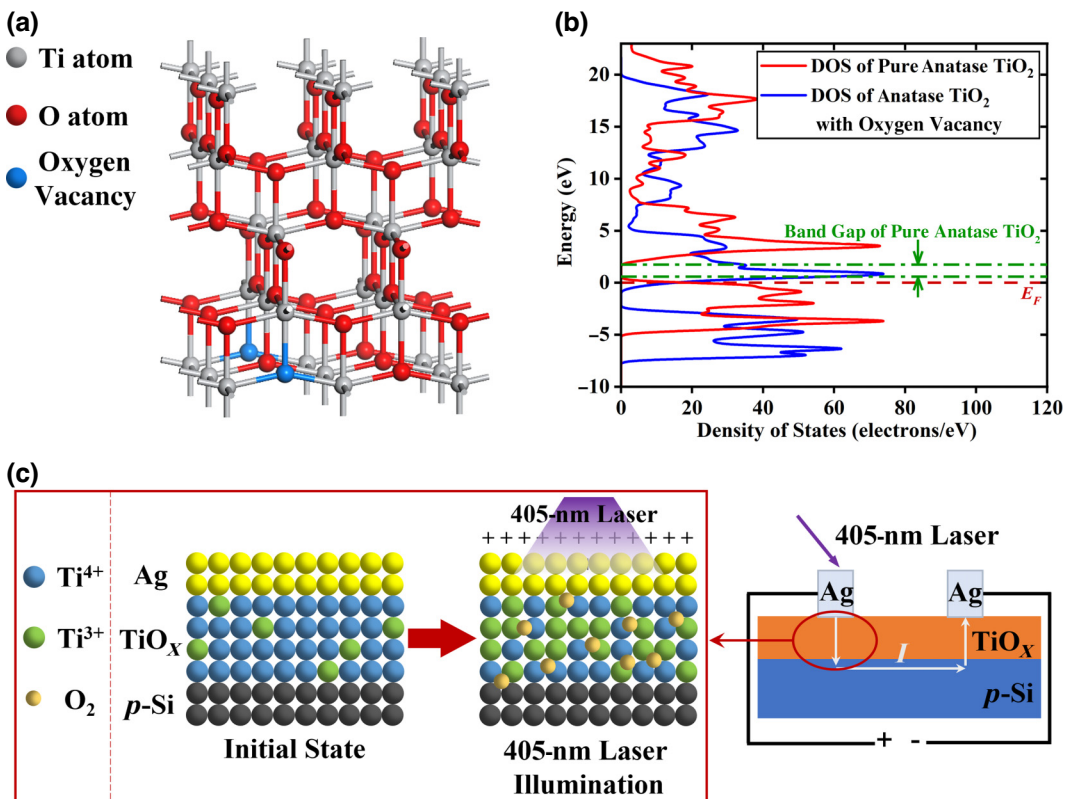


FIG. 2. (a) Structure of the anatase supercell of  $\text{Ti}_{16}\text{O}_{32}$ ; blue atoms are removed to form oxygen vacancies. (b) Results of the DFT calculations show the DOS of pure anatase  $\text{TiO}_2$  and the DOS of anatase  $\text{TiO}_2$  with oxygen vacancies. (c) Proposed switching mechanism in the  $\text{TiO}_x$ -based ORRAM.

analyzed intensively. The optical absorption gaps of anatase and rutile  $\text{TiO}_2$  films are found to be 3.2 and 3.0 eV, respectively, at room temperature [29], and the corresponding absorption wavelengths are 387 and 414 nm, respectively. However, our device is capable of absorbing 780-nm laser, indicating a change in the band gap of  $\text{TiO}_2$ . Using first-principles density-functional theory (DFT) [30,31] to calculate how oxygen vacancies influence the density of states (DOS) of anatase  $\text{TiO}_2$ , we can show why the absorption band is enlarged. Figure 2(a) shows the structure of the anatase supercell of  $\text{Ti}_{16}\text{O}_{32}$  used in the calculations, and the blue atoms are removed to form oxygen vacancies. Figure 2(b) shows the results of the calculation. The red curve is the DOS of pure anatase  $\text{TiO}_2$ , and the band gap obtained from the curve is 2.1 eV, which is much smaller than that found experimentally, 3.2 eV, as mentioned above. Such band-gap underestimation is inevitable in DFT calculations [32], but it does not prevent the semiquantitative understanding of how oxygen vacancies influence the band gap. The blue curve is the DOS of anatase  $\text{TiO}_2$  with oxygen vacancies, and it forms new energy levels in the band gap of pure anatase  $\text{TiO}_2$ . Therefore, oxygen vacancies in anatase  $\text{TiO}_2$  will narrow its band gap and the absorption band will be widened. A more detailed study

shows that, in the anatase  $\text{TiO}_2$ -based disordered layer, the band gap narrows to the range of 1.1–2.1 eV and the absorption band widens to the range of 400–900 nm [33].

In this work, the initial oxygen vacancies in the film make anatase  $\text{TiO}_2$  available to absorb light with a wavelength of 405–780 nm, thus producing the photogenerated carrier. Meanwhile, as the oxygen atoms are removed, the long-range order of the crystal will be destroyed. One removed lattice oxygen atom creates a point defect and three undercoordinated (fivefold) Ti ions ( $\text{Ti}_{5c}^{3+}$ ) [34]. This quantitative correspondence can also be confirmed from Fig. 2(a). At the same time, three dangling bonds are created, and the conductivity of the  $\text{TiO}_x$  film increases due to the higher concentrations of free electrons emerging from dangling bonds [35]. A mechanistic explanation is shown in Fig. 2(c). For the sake of simplicity, the annotation of the oxygen vacancy is ignored in the figure, and the corresponding  $\text{Ti}^{3+}$  is used for illustration. As mentioned above, there are already several oxygen vacancies in  $\text{TiO}_x$  in the initial state; these improve light absorption, then generate electrons and holes. The photogenerated electrons will react with the oxygen atoms in the lattice to produce oxygen ions ( $\text{O}^{2-}$ ) and oxygen vacancies ( $V_O^{2+}$ ), and the oxygen vacancies will be accompanied by two

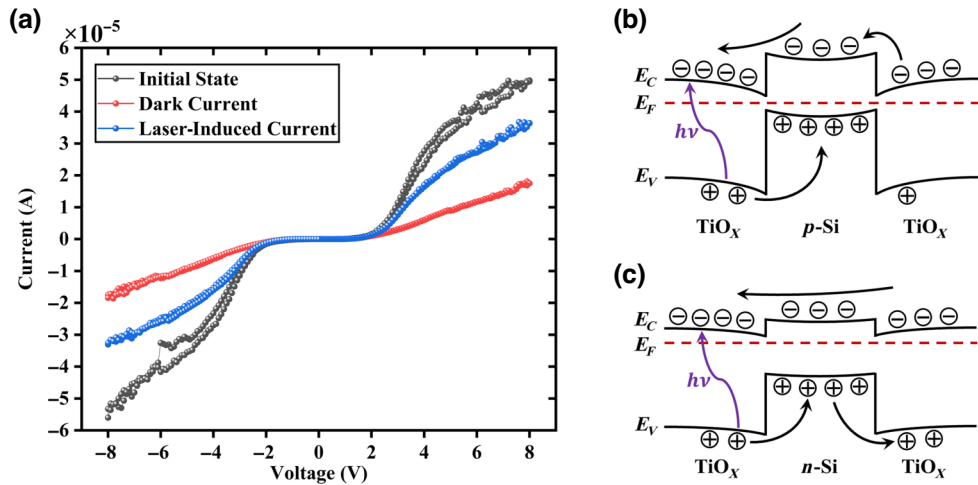


FIG. 3. (a)  $I$ - $V$  curves of the Ag/TiO<sub>x</sub>/n-Si structure before and after laser stimulation. Band-alignment analysis for (b)  $p$ -type silicon substrate and (c)  $n$ -type silicon substrate.

electrons to form the neutral oxygen vacancies ( $V_O^0$ ) [17]:  $O + 2e^- = V_O^0 + O^{2-}$ .

The neutral oxygen vacancies ( $V_O^0$ ) are always higher in energy than the single-electron-occupied oxygen vacancies ( $V_O^{1+}$ ) and the doubly ionized  $V_O^{2+}$  center [36]; thus, electrons are released during oxygen-vacancy formation. The electrons donated by these oxygen vacancies may be captured by the neighboring Ti interstitials ( $Ti^{4+}$ ) and form  $Ti^{3+}$  [35]:  $Ti^{4+} + e^- = Ti^{3+}$ .

As mentioned above, reduction of the Ti ions increases the concentration of free electrons in the TiO<sub>x</sub> film; thus, the conductivity of the device is increased. Meanwhile,  $O^{2-}$  ions free two electrons, which are transferred to an oxygen atom and released in the form of O<sub>2</sub> gas [15]. XPS analysis of the TiO<sub>x</sub> film with and without laser stimulation can be found in Fig. S3 within the Supplemental Material [18], which confirms the decrease of oxygen ions and the reduction of Ti ions.

The holes provided by the  $p$ -Si substrate also facilitate the above process, and Fig. 3(a) confirms that no significant increase in conductivity can be observed under laser stimulation if the device is based on the  $n$ -Si substrate. The rectification effect of the device (Fig. S4 within the Supplemental Material [18]) shows that, when a negative bias is applied to the laser-irradiated electrode, the holes provided by the  $p$ -Si substrate will be trapped near the negative electrode, so it is difficult to change the resistance state of the device. Therefore, the laser-induced resistive switching effect mentioned in this work is also regulated by  $p$ -type substrates. The above effect exhibits an insulator-to-metal transition characteristic, which is consistent with the properties of Mott insulators [37–39], and TiO<sub>2</sub> is one of the Mott insulators [40].

In addition, band alignment between the TiO<sub>x</sub> film and the  $p$ -type ( $n$ -type) Si substrate can also affect the above

effect, as shown in Fig. 3(b) [Fig. 3(c)]. When  $p$ -Si is used as the substrate, the conduction band and valence band of TiO<sub>x</sub> are much lower than those of  $p$ -Si. Therefore, when no laser is applied, the higher barrier makes it exhibit a very-large-resistance state. After applying laser stimulation, in addition to the resistance change effect caused by oxygen vacancies mentioned above, photogenerated carriers can further participate in the transmission of current and make a certain contribution to the increase in the current. When  $n$ -Si is used as the substrate, the conduction band of TiO<sub>x</sub> is very close to the conduction band of  $n$ -Si, and electrons can already conduct smoothly. As shown in Fig. 3(a), its conductivity is more than 1 order of magnitude higher than that of  $p$ -Si as the substrate. Therefore, the photogenerated carriers generated by laser stimulation not only contribute little to it, but may also reduce the conductivity of the device by filling the conduction band with excess electrons.

The next question to address is why the hysteretic characteristics appear under laser stimulation. When the positive electrode is stimulated by the 405-nm laser, the formation of oxygen vacancies and the release of O<sub>2</sub> gas, as described above, will occur, and the concentration of  $Ti^{3+}$  in the TiO<sub>x</sub> film will increase, resulting in a region of low resistance, as shown in Fig. 2(c). The current will pass longitudinally through the TiO<sub>x</sub> layer, then conduct to the area below the negative electrode through  $p$ -Si, finally passing through the TiO<sub>x</sub> layer to the Ag negative electrode. Figure S5 within the Supplemental Material [18] shows that the switching effect of the device hardly changes with the electrode spacing, confirming the current-conduction mode mentioned above. Meanwhile, the formation of oxygen vacancies and  $Ti^{3+}$  also occurs in the TiO<sub>x</sub> film below the negative electrode. Finally, the TiO<sub>x</sub> films below both electrodes are switched to low-resistance states, which make

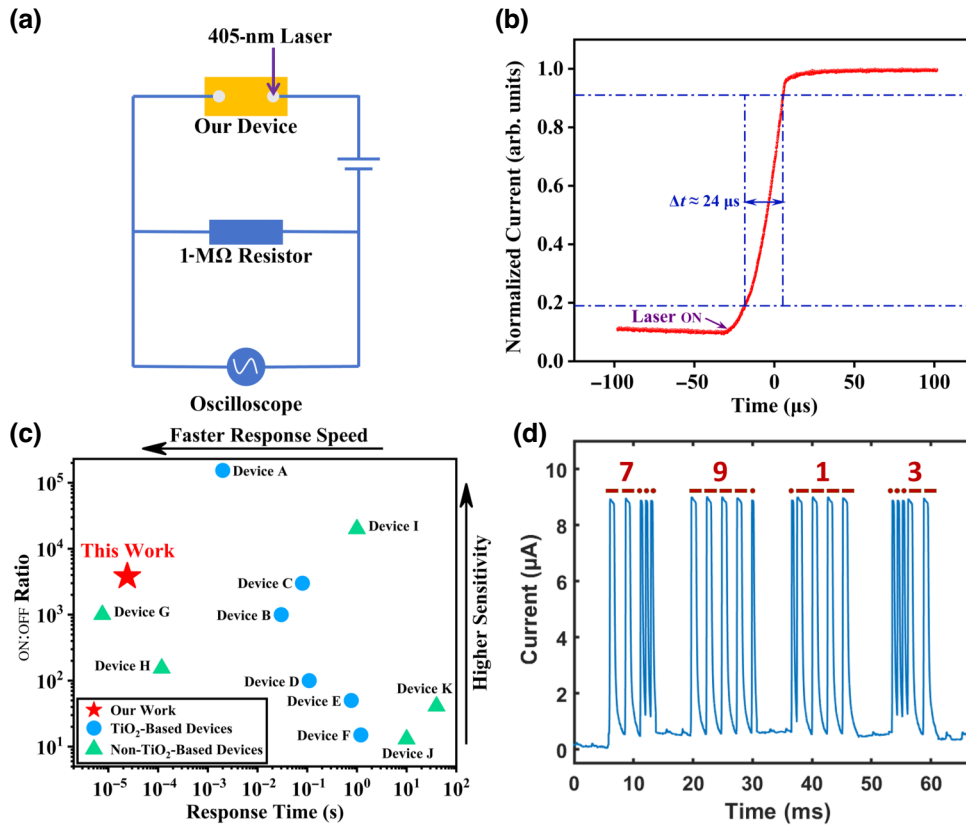


FIG. 4. (a) Schematic diagram of the homemade transient photoresponse measurement system. (b) Laser-pulse response measured for  $\text{Ag}/\text{TiO}_x/\text{p-Si}$  structures. (c) Response speed and ON:OFF ratio compared with the reported  $\text{TiO}_2$ -based photodetectors device A [44], device B [45], device C [46], device D [47], device E [48], and device F [49], and non- $\text{TiO}_2$ -based photodetector device G [50], device H [51], device I [52], device J [53], and device K [9]. (d) Morse code information transmission based on the fast optical response speed of the device.

the device show the hysteretic characteristics. It should be noted that, due to the instability of  $\text{Ti}^{3+}$  [41,42], after removing the laser, the photogenerated carriers in the film will recombine, and  $\text{Ti}^{3+}$  will react with the  $\text{O}_2$  retained in the lattice back to the  $\text{TiO}_2$  state, thus switching the device to a HRS.

The last question is why the resistance state of the dark current is even higher than the initial state. The explanation given herein is based on a Mott insulator [37–39]. It is found that, as the donor concentrations in anatase  $\text{TiO}_2$  film approaches  $10^{19} \text{ cm}^{-3}$ , a Mott (insulator-to-metal) transition occurs, but none of these effects are observed for the rutile film [29,43]. For the initial state, the point defects ( $\text{Ti}^{3+}$  interstitials or oxygen vacancies) in the  $\text{TiO}_x$  film are nearly uniformly distributed, and the resistance state of the device is almost completely dependent on the uniform  $\text{TiO}_x$  film. Under illumination, the defects caused by oxygen vacancies accumulate in larger quantities below the positive electrode than that below the negative electrode, and the increase in defect concentration makes the device switch to the LRS. After removing the laser, the unstable  $\text{Ti}^{3+}$  will

be oxidized on the basis of the nonuniform distribution. Then the concentration of residual defects near the positive electrode will exceed that near the negative electrode, which in the circuit is equivalent to a region of metal phase in series with a region of insulator phase. Therefore, the resistance of the device after removing illumination will be higher than the initial state.

#### D. Response-time analysis and Morse code transmission

The speed of switching is a crucial factor for memory applications. As the resistance state of the device varies from  $10^7$  to  $10^4 \Omega$ , when a  $1-\text{M}\Omega$  resistor is connected in series in the circuit, the partial voltage on it will change significantly as the resistance of the device changes. Using an oscilloscope to detect voltage changes in the resistor, Fig. 4(a) shows a schematic diagram of the testing method. The test uses a 405-nm laser pulse of  $800 \mu\text{s}$ . As the laser stimulates the sample, it can be observed that the resistance value of the device switches within  $24 \mu\text{s}$ , as shown in Fig. 4(b). With shorter laser pulses, faster

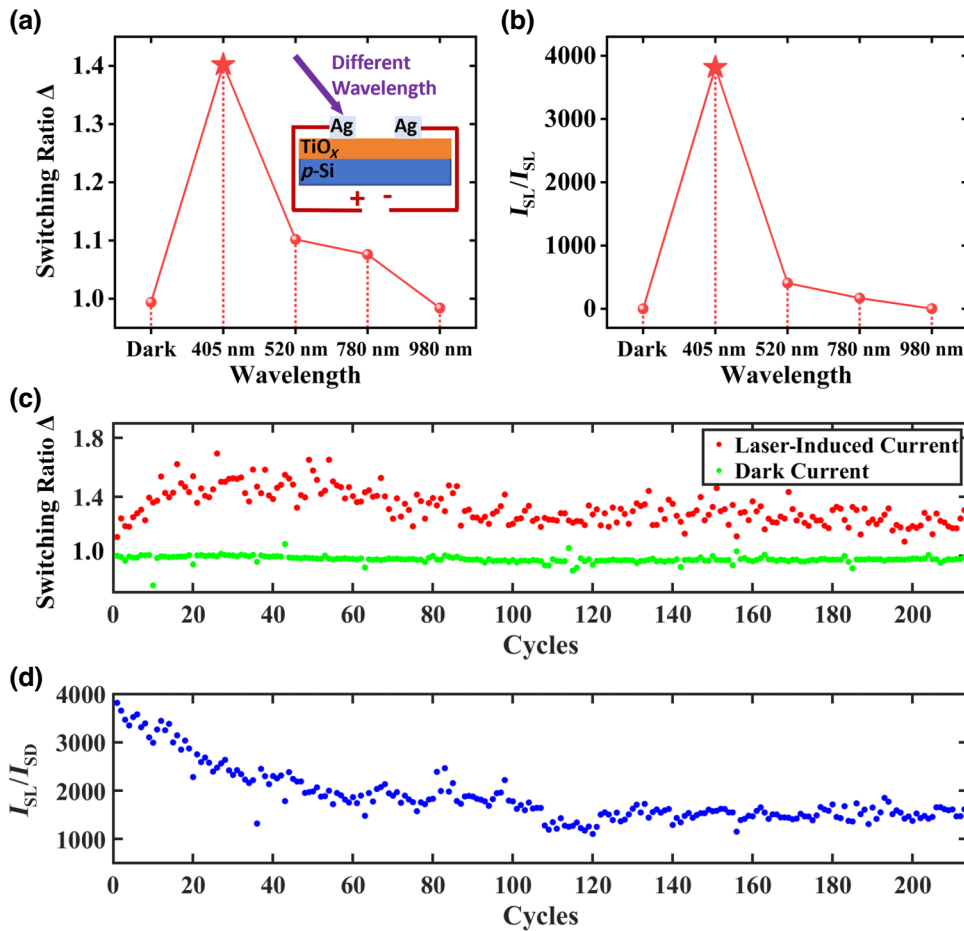


FIG. 5. Resistive switching characteristics of  $\text{Ag}/\text{TiO}_x/\text{p-Si}$  structures. (a) Switching ratio,  $\Delta$ , under different wavelengths of laser stimulation. (b) Laser-to-dark ratio,  $I_{SL}/I_{SD}$ , under different wavelengths of laser stimulation. (c) Variation of the switching ratio,  $\Delta$ , of the laser-induced current and of the dark current during 210 cycles. (d) Variation of  $I_{SL}/I_{SD}$  during 210 cycles.

response times may be obtained. For general  $\text{TiO}_2$ -based photodetectors, the response time always varies from milliseconds to seconds, which is far slower than that in our work, as shown in Fig. 4(c) (devices A–F). And the ON:OFF ratio of our device is also at a high level among  $\text{TiO}_2$ -based photodetectors, exceeding  $10^3$ . Even compared to some of the current mainstream optoelectronic

devices reported with the potential for application in neuromorphic vision sensors [devices G–J in Fig. 4(c)], the performance of our devices is superior. The laser-induced resistive switching effect proposed in this work uses a laser to induce oxygen vacancies, and the generated oxygen vacancies further improve light absorption, thus greatly improving the response speed of the device to the laser and

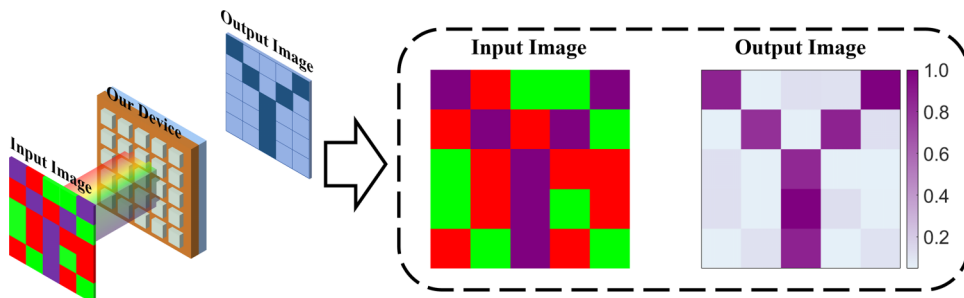


FIG. 6. Schematic diagram of an imaging system by using a device array to detect letter patterns with noise, and the image of the letter “Y” obtained from the imaging system.

presenting a resistive switching effect under stimulation by the laser.

Using the fast optical response performance of our device, we propose an idea to apply it to fast information transmission. We use the length of the laser-pulse width to represent a sequence of two communication states, where the short duration stands for “0” or a dot and long duration represents “1” or a dash, thus using optical signals to represent Morse code. After receiving encoded optical signals using our device, it quickly converts them into the corresponding electrical signals, enabling fast optical communication. Figure 4(d) shows the fast transmission of Morse code for the digital information “7913,” completing the transmission of four characters in 60 ms, much faster than the previously reported transmission of one character in approximately 20 s [51]. The above case shows that our device has great potential for application in optical wireless communication for a human-machine interface.

### E. Device-reliability analysis and potential applications in image processing

More resistive switching characteristics are also tested to show the reliability of the effects. Figure 5(a) shows the switching ratio,  $\Delta$ , of the Ag/TiO<sub>x</sub>/p-Si structure under different wavelengths of laser stimulation. All lasers used here have a power of 2 mW/cm<sup>2</sup>. And the laser-to-dark ratio,  $I_{SL}/I_{SD}$ , is shown in Fig. 5(b). The switching ratio,  $\Delta$ , of 405-nm laser stimulation is about 1.4, much higher than the others. And it also has the largest  $I_{SL}/I_{SD}$ , which is about  $4 \times 10^3$ . For the 520- and 780-nm lasers, the optical absorption of the device decreases, thus  $I_{SL}/I_{SD}$  goes down. The 980-nm laser stimulation has little effect on the switching ratio,  $\Delta$ , and its  $I_{SL}$  is very low, which means that the device almost does not absorb the 980-nm laser.

The endurance of the device with the Ag/TiO<sub>x</sub>/p-Si structure is tested. The variation of the switching ratio,  $\Delta$ , in 210 consecutive cycles is shown in Fig. 5(c). In 210 cycles, the dark current always fails to produce the resistive switching effect, for its switching ratio,  $\Delta$ , is always around 1. However, under 405-nm laser stimulation, the device exhibits good resistive switching characteristics. With the progress of the cycle, the switching ratio of the device increases slightly at first, and then falls back to 1.3 for fluctuations. The laser-to-dark ratio,  $I_{SL}/I_{SD}$ , can also be calculated, and its fluctuation is shown in Fig. 5(d). It can be seen that it starts at  $4 \times 10^3$  and slowly decreases, eventually settling at a level above  $1 \times 10^3$ . Due to the continuous progress of the test, some oxygen-vacancy defects will slowly accumulate in the TiO<sub>x</sub> layer, which can still remain even after the laser is removed, thus slightly increasing the value of the dark current, and finally reducing  $I_{SL}/I_{SD}$  to a level of around  $1 \times 10^3$ . The results shown above can demonstrate the stability and repeatability of the device.

By utilizing the reliable durability of the device and its extremely sensitive response characteristics to the 405-nm wavelength laser, we propose applying it to the image-processing field of color-noise reduction. Lasers at three wavelengths of 405, 520, and 780 nm are used as the three basic colors of purple, green, and red for image input, where the effective information of the image consists of purple pixels, with green and red as random noise inputs. The device was fixed on a probe station to receive the image information, and the current of each pixel was then recorded and the two-dimensional patterns of the image were output by the MATLAB software. Because the device’s response at 405 nm is much more sensitive than its response at 520 and 780 nm, the green and red noise information is effectively filtered, leaving clear purple pixels forming the image. Figure 6 shows the images before and after processing with the device. It can be seen that the noise in the input image is well filtered, and the letter “Y” in the output image is clearly visible. The above case indicates the promising application of the device in the field of optoelectronic imaging.

## IV. CONCLUSION

By using the photosensitive properties of TiO<sub>2</sub> and the effects of the oxygen vacancy in anatase TiO<sub>2</sub>, we unambiguously obtain a laser-induced resistive switching device with remarkable effects. The device with a structure of Ag/TiO<sub>x</sub>/p-Si is simply fabricated, highly photosensitive, and extremely durable, and it exhibits an enhancement in electrical conductivity of  $10^3$  times with a response time of less than 24  $\mu$ s and a large resistive switching ratio under laser stimulation. We take advantage of the excellent optical response performance of this device to demonstrate its application prospects in the fields of fast optical communication and image processing. The excellent performance and the clear laser-control mechanism of the device open the way to promote the practical application of ORRAM.

## ACKNOWLEDGMENTS

This work is supported by the National Natural Science Foundation of China under Grants No. 11374214 and No. 10974135.

- 
- [1] L. O. Chua, Memristor—the missing circuit element, *IEEE Trans. Circuit Theory* **18**, 507 (1971).
  - [2] P. Grunberg, R. Schreiber, Y. Pang, M. B. Brodsky, and H. Sowers, Layered magnetic structures: Evidence for anti-ferromagnetic coupling of Fe layers across Cr interlayers, *Phys. Rev. Lett.* **57**, 2442 (1986).
  - [3] M. N. Baibich, J. M. Broto, A. Fert, F. N. Van Dau, F. Petroff, P. Etienne, G. Creuzet, A. Friederich, and J. Chazelas, Giant magnetoresistance of (001)Fe/(001)Cr magnetic superlattices, *Phys. Rev. Lett.* **61**, 2472 (1988).

- [4] F. Pan, S. Gao, C. Chen, C. Song, and F. Zeng, Recent progress in resistive random access memories: Materials, switching mechanisms, and performance, *Mater. Sci. Eng., R* **83**, 1 (2014).
- [5] M. Lanza, H. S. P. Wong, E. Pop, D. Ielmini, D. Strukov, B. C. Regan, L. Larcher, M. A. Villena, J. J. Yang, L. Goux, *et al.*, Recommended methods to study resistive switching devices, *Adv. Electron. Mater.* **5**, 1800143 (2019).
- [6] X. Huang, K. A. Jiang, Y. R. Niu, R. Z. Wang, D. Y. Zheng, A. H. Dong, X. Y. Dong, C. L. Mei, J. Lu, S. Liu, *et al.*, Configurable ultra-low operating voltage resistive switching between bipolar and threshold behaviors for Ag/TaO<sub>x</sub>/Pt structures, *Appl. Phys. Lett.* **113**, 112103 (2018).
- [7] M.-J. Lee, C. B. Lee, D. Lee, S. R. Lee, M. Chang, J. H. Hur, Y.-B. Kim, C.-J. Kim, D. H. Seo, S. Seo, *et al.*, A fast, high-endurance and scalable non-volatile memory device made from asymmetric Ta<sub>2</sub>O<sub>5-x</sub>/TaO<sub>2-x</sub> bilayer structures, *Nat. Mater.* **10**, 625 (2011).
- [8] N. Raeis-Hosseini, S. Lim, H. Hwang, and J. Rho, Reliable Ge<sub>2</sub>Sb<sub>2</sub>Te<sub>5</sub>-integrated high-density nanoscale conductive bridge random access memory using facile nitrogen-doping strategy, *Adv. Electron. Mater.* **4**, 1800360 (2018).
- [9] F. Zhou, Z. Zhou, J. Chen, T. H. Choy, J. Wang, N. Zhang, Z. Lin, S. Yu, J. Kang, H. P. Wong, *et al.*, Optoelectronic resistive random access memory for neuromorphic vision sensors, *Nat. Nanotechnol.* **14**, 776 (2019).
- [10] X. Fu, T. Li, B. Cai, J. Miao, G. N. Panin, X. Ma, J. Wang, X. Jiang, Q. Li, Y. Dong, *et al.*, Graphene/MoS<sub>2-x</sub>O<sub>x</sub>/graphene photomemristor with tunable non-volatile responsivities for neuromorphic vision processing, *Light: Sci. Appl.* **12**, 39 (2023).
- [11] L. G. Zhu, J. Zhou, Z. L. Guo, and Z. M. Sun, An overview of materials issues in resistive random access memory, *J. Materomics* **1**, 285 (2015).
- [12] R. Waser, R. Dittmann, G. Staikov, and K. Szot, Redox-based resistive switching memories - nanoionic mechanisms, prospects, and challenges, *Adv. Mater.* **21**, 2632 (2009).
- [13] I. Valov, E. Linn, S. Tappertzhofen, S. Schmelzer, J. van den Hurk, F. Lentz, and R. Waser, Nanobatteries in redox-based resistive switches require extension of memristor theory, *Nat. Commun.* **4**, 1771 (2013).
- [14] A. Mottaghizadeh, Q. Yu, P. L. Lang, A. Zimmers, and H. Aubin, Metal oxide resistive switching: Evolution of the density of states across the metal-insulator transition, *Phys. Rev. Lett.* **112**, 066803 (2014).
- [15] A. Hazra, A. Jan, A. Tripathi, S. Kundu, P. K. R. Boppidi, and S. Gangopadhyay, Optimized resistive switching in TiO<sub>2</sub> nanotubes by modulation of oxygen vacancy through chemical reduction, *IEEE Trans. Electron Devices* **67**, 2197 (2020).
- [16] A. Barman, C. P. Saini, P. K. Sarkar, G. Bhattacharjee, G. Bhattacharya, S. Srivastava, B. Satpati, D. Kanjilal, S. K. Ghosh, S. Dhar, *et al.*, Resistive switching behavior in oxygen ion irradiated TiO<sub>2-x</sub> films, *J. Phys. D: Appl. Phys.* **51**, 065306 (2018).
- [17] R. Zhang, H. Huang, Q. Xia, C. Ye, X. Wei, J. Wang, L. Zhang, and L. Q. Zhu, Role of oxygen vacancies at the TiO<sub>2</sub>/HfO<sub>2</sub> interface in flexible oxide-based resistive switching memory, *Adv. Electron. Mater.* **5**, 1800833 (2019).
- [18] See the Supplemental Material at <http://link.aps.org-supplemental/10.1103/PhysRevApplied.22.014031> for details of device fabrication, transmittance of Ag electrodes, photoelectric properties of the *p*-Si substrate, XPS analysis of TiO<sub>x</sub> thin films, and additional testing of the device performance. It also contains Refs. [19,20].
- [19] C. M. Wang and S. Y. Lin, Electrochromic properties of sputtered TiO<sub>2</sub> thin films, *J. Solid State Electrochem.* **10**, 255 (2005).
- [20] S. H. Kang, J.-W. Lim, H. S. Kim, J.-Y. Kim, Y.-H. Chung, and Y.-E. Sung, Photo and electrochemical characteristics dependent on the phase ratio of nanocolumnar structured TiO<sub>2</sub> films by rf magnetron sputtering technique, *Chem. Mater.* **21**, 2777 (2009).
- [21] U. Balachandran and N. G. Eror, Raman spectra of titanium dioxide, *J. Solid State Chem.* **42**, 276 (1982).
- [22] J. Yan, G. Wu, N. Guan, L. Li, Z. Li, and X. Cao, Understanding the effect of surface/bulk defects on the photocatalytic activity of TiO<sub>2</sub>: Anatase versus rutile, *Phys. Chem. Chem. Phys.* **15**, 10978 (2013).
- [23] G. A. Tompsett, G. A. Bowmaker, R. P. Cooney, J. B. Metson, K. A. Rodgers, and J. M. Seakins, The Raman spectrum of brookite, TiO<sub>2</sub> (*Pbca*, *Z* = 8), *J. Raman Spectrosc.* **26**, 57 (1995).
- [24] Z. Kou, A. Hashemi, M. J. Puska, A. V. Krasheninnikov, and H.-P. Komsa, Simulating Raman spectra by combining first-principles and empirical potential approaches with application to defective MoS<sub>2</sub>, *npj Comput. Mater.* **6**, 59 (2020).
- [25] L. O. Chua and S. M. Kang, Memristive devices and systems, *Proc. IEEE* **64**, 209 (1976).
- [26] Y. V. Pershin and M. Di Ventra, Memory effects in complex materials and nanoscale systems, *Adv. Phys.* **60**, 145 (2011).
- [27] A. Dong, K. Chang, R. Wang, D. Zheng, and H. Wang, Modulation of optical switching characteristics in MoS<sub>2</sub>/HfO<sub>2</sub>/*p*-Si structures, *Appl. Phys. Lett.* **117**, 072104 (2020).
- [28] X. Long, H. Tan, F. Sánchez, I. Fina, and J. Fontcuberta, Non-volatile optical switch of resistance in photoferroelectric tunnel junctions, *Nat. Commun.* **12**, 382 (2021).
- [29] H. Tang, K. Prasad, R. Sanjinès, P. E. Schmid, and F. Lévy, Electrical and optical properties of TiO<sub>2</sub> anatase thin films, *J. Appl. Phys.* **75**, 2042 (1994).
- [30] P. Hohenberg and W. Kohn, Inhomogeneous electron gas, *Phys. Rev.* **136**, B864 (1964).
- [31] M. D. Segall, P. J. D. Lindan, M. J. Probert, C. J. Pickard, P. J. Hasnip, S. J. Clark, and M. C. Payne, First-principles simulation: Ideas, illustrations and the CASTEP code, *J. Phys.: Condens. Matter* **14**, 2717 (2002).
- [32] J. P. Perdew, Density functional theory and the band gap problem, *Int. J. Quantum Chem.* **28**, 497 (1985).
- [33] H. Tan, Z. Zhao, M. Niu, C. Mao, D. Cao, D. Cheng, P. Feng, and Z. Sun, A facile and versatile method for preparation of colored TiO<sub>2</sub> with enhanced solar-driven photocatalytic activity, *Nanoscale* **6**, 10216 (2014).

- [34] C. Di Valentin, G. Pacchioni, and A. Selloni, Reduced and *n*-type doped TiO<sub>2</sub>: Nature of Ti<sup>3+</sup> species, *J. Phys. Chem. C* **113**, 20543 (2009).
- [35] D. Acharyya, A. Hazra, and P. Bhattacharyya, A journey towards reliability improvement of TiO<sub>2</sub> based resistive random access memory: A review, *Microelectron. Reliab.* **54**, 541 (2014).
- [36] A. Janotti, J. B. Varley, P. Rinke, N. Umezawa, G. Kresse, and C. G. Van de Walle, Hybrid functional studies of the oxygen vacancy in TiO<sub>2</sub>, *Phys. Rev. B* **81**, 085212 (2010).
- [37] N. F. Mott, The basis of the electron theory of metals, with special reference to the transition metals, *Proc. Phys. Soc. A* **62**, 416 (1949).
- [38] N. F. Mott, Electrons in disordered structures, *Adv. Phys.* **16**, 49 (1967).
- [39] N. F. Mott, The transition to the metallic state, *Philos. Mag.* **6**, 287 (1961).
- [40] G. Zhou, Z. Wang, B. Sun, F. Zhou, L. Sun, H. Zhao, X. Hu, X. Peng, J. Yan, H. Wang, *et al.*, Volatile and non-volatile memristive devices for neuromorphic computing, *Adv. Electron. Mater.* **8**, 2101127 (2022).
- [41] M. Y. Kang, H. J. Yun, S. Yu, W. Kim, N. D. Kim, and J. Yi, Effect of TiO<sub>2</sub> crystalline phase on CO oxidation over CuO catalysts supported on TiO<sub>2</sub>, *J. Mol. Catal. A: Chem.* **368–369**, 72 (2013).
- [42] G.-H. Han, G. P. Lee, and K.-Y. Lee, Crystal refinement of rutile by sonochemical method to achieve high performance Pd catalysts for direct synthesis of hydrogen peroxide, *Catal. Today* **352**, 262 (2020).
- [43] A. Wahl and J. Augustynski, Charge carrier transport in nanostructured anatase TiO<sub>2</sub> films assisted by the self-doping of nanoparticles, *J. Phys. Chem. B* **102**, 7820 (1998).
- [44] J. Xu, W. Yang, H. Chen, L. Zheng, M. Hu, Y. Li, and X. Fang, Efficiency enhancement of TiO<sub>2</sub> self-powered UV photodetectors using a transparent Ag nanowire electrode, *J. Mater. Chem. C* **6**, 3334 (2018).
- [45] Y. Xie, L. Wei, Q. Li, Y. Chen, H. Liu, S. Yan, J. Jiao, G. Liu, and L. Mei, A high performance quasi-solid-state self-powered UV photodetector based on TiO<sub>2</sub> nanorod arrays, *Nanoscale* **6**, 9116 (2014).
- [46] X. Li, C. Gao, H. Duan, B. Lu, Y. Wang, L. Chen, Z. Zhang, X. Pan, and E. Xie, High-performance photoelectrochemical-type self-powered UV photodetector using epitaxial TiO<sub>2</sub>/SnO<sub>2</sub> branched heterojunction nanostucture, *Small* **9**, 2005 (2013).
- [47] B. Liu, X. Xu, M. Han, H. Cheng, J. Chen, X. Sun, Q. Zhang, X. Duan, and J. Hu, Schottky junction made from a nanoporous Au and TiO<sub>2</sub> film for plasmonic photodetectors, *ACS Appl. Nano Mater.* **6**, 4619 (2023).
- [48] Y. Zhang, W. Xu, X. Xu, W. Yang, S. Li, J. Chen, and X. Fang, Low-cost writing method for self-powered paper-based UV photodetectors utilizing Te/TiO<sub>2</sub> and Te/ZnO heterojunctions, *Nanoscale Horiz.* **4**, 452 (2019).
- [49] L. Zheng, F. Teng, Z. Zhang, B. Zhao, and X. Fang, Large scale, highly efficient and self-powered UV photodetectors enabled by all-solid-state *n*-TiO<sub>2</sub> nanowell/*p*-NiO mesoporous nanosheet heterojunctions, *J. Mater. Chem. C* **4**, 10032 (2016).
- [50] Y. Zhan, Z. Wu, P. Zeng, W. Wang, Y. Jiang, H. Zheng, P. Zheng, L. Zheng, and Y. Zhang, High-performance self-powered WSe<sub>2</sub>/ReS<sub>2</sub> photodetector enabled via surface charge transfer doping, *ACS Appl. Mater. Interfaces* **15**, 55043 (2023).
- [51] S. Feng, J. Li, L. Feng, Z. Liu, J. Wang, C. Cui, O. Zhou, L. Deng, H. Xu, B. Leng, *et al.*, Dual-mode conversion of photodetector and neuromorphic vision sensor via bias voltage regulation on a single device, *Adv. Mater.* **35**, 2308090 (2023).
- [52] A. Dodda, D. Jayachandran, A. Pannone, N. Trainor, S. P. Stepanoff, M. A. Steves, S. S. Radhakrishnan, S. Bachu, C. W. Ordonez, J. R. Shallenberger, *et al.*, Active pixel sensor matrix based on monolayer MoS<sub>2</sub> phototransistor array, *Nat. Mater.* **21**, 1379 (2022).
- [53] H. L. Park, H. Kim, D. Lim, H. Zhou, Y. H. Kim, Y. Lee, S. Park, and T. W. Lee, Retina-inspired carbon nitride-based photonic synapses for selective detection of UV light, *Adv. Mater.* **32**, 1906899 (2020).